Int J Adv Manuf Technol (2017) 88:1175–1185
DOI 10.1007/s00170-016-8826-7

ORIGINAL ARTICLE

Numerical and experimental investigation of inward tube electromagnetic forming

Hossein Ebrahimi Haratmeh[1] · **Alireza Fallahi Arezoodar**[1] · **Mohmoud Farzin**[2]

Received: 24 August 2015 / Accepted: 25 April 2016 / Published online: 7 May 2016

Abstract In this work, experimental and numerical simulation of high-speed inward forming of tubes on a die in electromagnetic forming (EMF) system using a compression coil is presented. A 2D axi-symmetric electromagnetic model is used to calculate magnetic field and magnetic forces. Modified loose-coupled simulations of electromagnetic and structural aspects of EMF process are reported and emphasized in this paper. During the simulation, in each time step, the transient magnetic forces are obtained from the electromagnetic model and used as input load to the mechanical model. Based on the calculated deformation, in each step, the tube geometry in the electromagnetic model is updated to calculate the electromagnetic forces in proceeding step. Tube material, AA 6061-T6, is assumed to obey the Johnson-Cook (J-C) rate-dependent model. Displacement and thickness variations of workpieces along the tube length are presented and discussed experimentally and numerically. The results demonstrate that various workpiece zones could be thickened or thinned based on various process parameters. In addition, it is seen that the increase of discharge voltage decreases the thickness at die radius and reverses the thickening trend at tip of the bead.

Keywords High velocity forming · Electromagnetic forming · Inward tube forming · Johnson-Cook material model · Aluminum alloy

✉ Alireza Fallahi Arezoodar
afallahi@aut.ac.ir

[1] Department of Mechanical Eng, Amirkabir University of Technology, Tehran, Iran

[2] Department of Mechanical Eng, Isfahan University of Technology, Isfahan, Iran

1 Introduction

As a high energy rate forming (HERF), electromagnetic forming (EMF) uses Lorentz body forces to fabricate metallic parts [1]. Electromagnetic forming is a metal forming process that relies on the use of electromagnetic forces to deform metallic workpieces at high speeds, in the order of 100 m/s in less than 0.1 ms [2]. In this process, a transient electric current is induced in a coil using a capacitor bank and a high-speed switch. This current induces a magnetic field that penetrates the nearby conductive workpiece where an eddy current is generated. The magnetic field, together with the eddy current, induces Lorentz forces that drive the deformation of the workpiece.

High energy rate forming processes such as explosive forming and EMF have some attractive characteristics, such as extremely high ductility under high velocity conditions, the low spring back after the unloaded condition, and the one-sided die which can be a male or a female die. Compared with other HERF processes, in EMF it is very easy to control the energy, little time is needed to form the products, it needs no transfer medium to transfer the deformation force, and it can reduce undesirable phenomena like spring back and wrinkling [3]. Because of higher strain rate and inertial stabilization of material failure modes, EMF can significantly increase formability in low ductility materials [4], with aluminum prominently among them [5]. One of the drawbacks of EMF is low efficiency due to low electrical conductivity of the object to deform. In order to improve the surface conductivity, coating of workpiece was proposed and an increasing of deformation was obtained [6].

Since it is difficult to control the energy in the HERF processes, it is not an easy task to make various complicated parts. Therefore many investigations have been conducted to obtain optimal process parameters and produce parts used in

the automobile and aerospace industry [3]. EMF process applications include automotive, ordnance, electrical equipment, office machinery, appliance, etc. [7]. Some operations such as flat sheet metal forming, ring compression, or expansion and assembly are made possible using this technology [8].

Several attempts have been made to model the EMF of alloys numerically. Among them, a comprehensive review and assessment of the EMF process has been presented by Mamalis et al. [9] and Psyk et al. [10]. Due to analytical difficulties arising in the mathematical treatment of an EMF process, numerical analysis has been extensively used [8, 10–12]. Although sophisticated finite element (FE) codes have been developed to simulate EMF process [13, 14], simple models have also been presented which give acceptable results [8, 15–17]. In these simple models, an EMF sheet process is treated as a combination of two uncoupled and independent problems: an electromagnetic problem and a forming problem. For instance, in a work performed by Imbert et al. [15], the magnetic pressure distribution that had been estimated from the analytical work of Al-Hassani [18] was used as a load in the forming simulation using ABAQUS code. It should be noted that other researchers, who have treated the EMF process from the manufacturers' point of view, have used approximate calculations to predict the magnetic pressure and then they have proceeded with the numerical simulation of the forming process by employing the commercial FEM codes such as MARC, LS-DYNA, ANSYS Mechanical, and Pam-Stamp2G [9]. Furthermore, some researchers have utilized a commercial software such as Maxwell to simulate electromagnetic aspects of EMF and another software like ABAQUS to simulate forming aspects of EMF [8, 19–21]. For instance Oliveira et al. [4] developed a "loosely coupled" model to simulate sheet EMF process. They combined a three-dimensional electromagnetic FE analysis using ANSYS code in conjunction with a structural analysis using explicit dynamic FE code LS-DYNA, to simulate the thermo-mechanical behavior of a metal sheet.

Haiping et al. [22] presented a sequential coupling simulation for electromagnetic tube compression by using finite element software ANSYS. In this method, the effect of tube deformation on the electromagnetic geometry was taken into account in electromagnetic model, by which the simulation accuracy was improved. Then some researchers used this algorithm [21, 23, 24]. Bartels et al. [23] presented a comparison for the electromagnetic tube compression of a custom loose-coupled simulation model and a more accurate sequential coupled approach. They deduced that deviations between the two simulation models increase with time, so that the loose-coupled approach leads to an overestimation of the final deformation. They found that the displacement predicted by the loose-coupled model is 30 % greater than the more accurate sequential coupled one at the end of simulation.

During recent years, several numerical studies have been conducted for the EMF process, a few of which are related to inward tube electromagnetic forming process. For example,

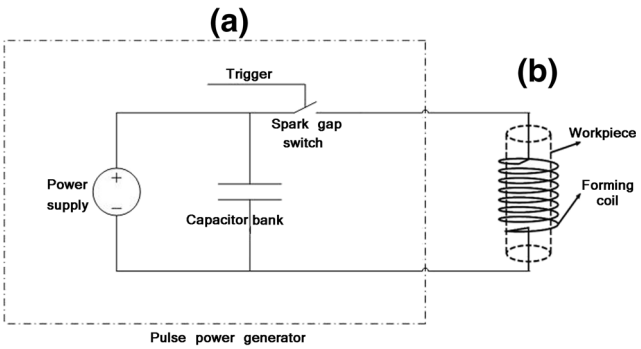

Fig. 1 Schematic of the EMF system for a tubular workpiece

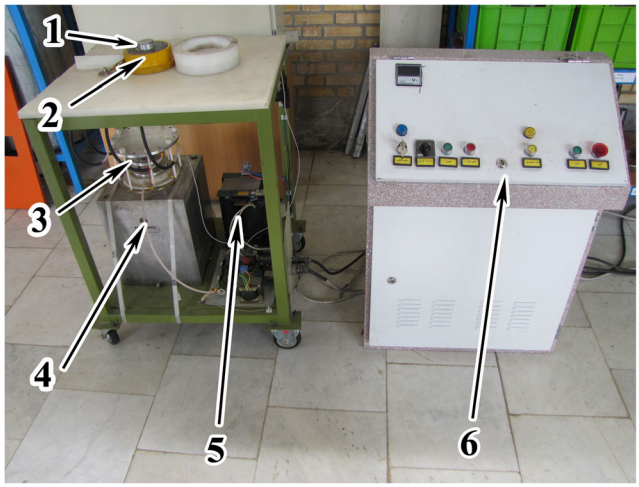

Fig. 2 Experimental test setup of EMF process

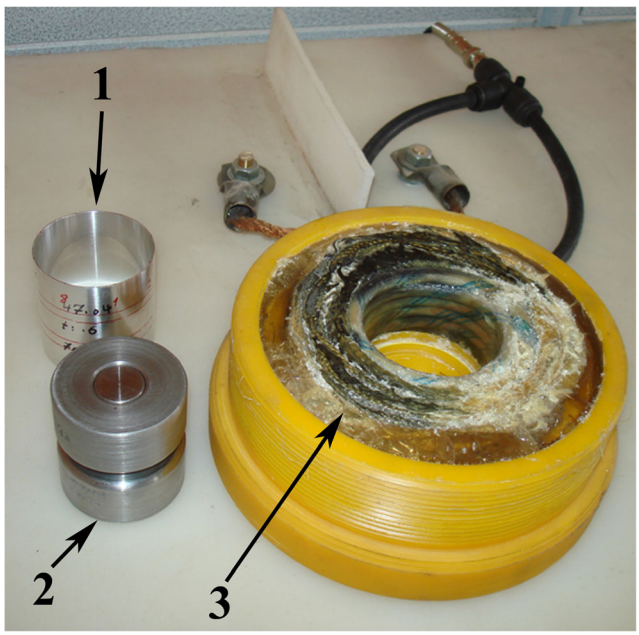

Fig. 3 Workpiece (*1*), die (*2*), and C53 coil (*3*) in the experimental setup

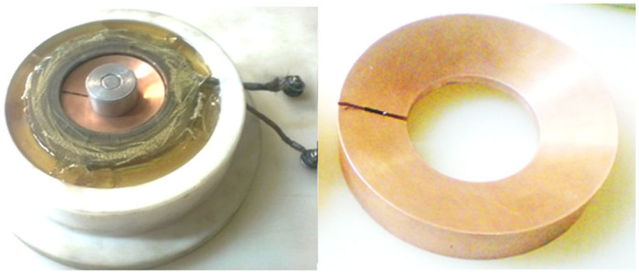

Fig. 4 Experimental setup of C100 coil with conical field shaper

Vivek et al. [25] studied the electromagnetic compression of steel tubes experimentally and numerically, by investigating buckling in the tube compression. They found that either increasing the forming energy or reducing compressed length can effectively increase the extent of diameter reduction. Murakoshi et al. [3] also studied inward bead forming of aluminum tubes by EMF. They concluded that over a certain discharge voltage, the bead depth and thickness strain at the tip of the bead increase rapidly. In the recent work of Fallahi et al. [26], effects of coil parameters on the bead shape in electromagnetic inward tube forming have been examined. In none of these works, thickness variations and displacements have been studied in detail.

In this work, an inward tube forming of 6061-T6 aluminum alloy tubes by EMF is studied numerically and experimentally. Modified loose-coupled approach is used to simulate this EMF process. In this method, the effect of tube geometry change on the electromagnetic pressure calculation is taken into account. Radial and thickness strain in FE analysis at the tip of the bead are studied and compared with experimental results. Thickness variations along the tube length are investigated both numerically and experimentally. Furthermore, variations of thickness and radial strain with an increase of discharge voltage are studied.

2 Theory

A schematic illustration of the apparatus for the electromagnetic tube compression is shown in Fig. 1. It consists of two parts: (a) control system including power supply, spark gap switch, and a capacitor bank; and (b) workpiece and die with a forming coil.

The fundamental equations of magnetic field within a conducting medium are as follows [11]

$$\nabla.\mathbf{J} = 0 \tag{1}$$

$$\nabla \times \mathbf{H} = \mathbf{J} \tag{2}$$

$$\nabla \times \mathbf{E} = -\frac{\partial \mathbf{B}}{\partial t} \tag{3}$$

$$\nabla.\mathbf{B} = 0 \tag{4}$$

$$\mathbf{B} = \mu \mathbf{H} \tag{5}$$

$$\mathbf{J} = \sigma_w(\mathbf{E} + \upsilon \times \mathbf{B}) \tag{6}$$

where ∇ are divergence and curl operator in Eqs. (1) and (2), respectively, $\mathbf{J}$ is current density, $\mathbf{H}$ is magnetic intensity, $\mathbf{E}$ is electric field, $\mathbf{B}$ is magnetic flux density, μ is permeability, σ_w is electric conductivity of the workpiece, ν is velocity of medium, and t is time. The first four equations are Maxwell's equations and Eqs. (5) and (6) are constitutive equations. If velocity term does not affect the magnetic field in these equations during the process [8] and a cylindrical coordinate system is applied for the tube, then the magnetic field density $\mathbf{B}$ possesses a radial component B_r and axial component B_z which are given as follows:

$$\begin{aligned} -\frac{1}{\mu_0\sigma_w}\left(\frac{\partial^2}{\partial r^2}+\frac{1}{r}\frac{\partial}{\partial r}+\frac{\partial^2}{\partial z^2}-\frac{1}{r^2}\right)B_r+\frac{\partial B_r}{\partial t}=0 \\ -\frac{1}{\mu_0\sigma_w}\left(\frac{\partial^2}{\partial r^2}+\frac{1}{r}\frac{\partial}{\partial r}+\frac{\partial^2}{\partial z^2}\right)B_z+\frac{\partial B_z}{\partial t}=0 \end{aligned} \tag{7}$$

where σ_w is conductivity of the workpiece and μ_0 is air permeability.

Assuming axi-symmetric conditions, eddy current has only a circumferential component which is given by

$$J_\theta = \frac{1}{\mu_0}\left(\frac{\partial B_r}{\partial z}+\frac{\partial B_z}{\partial r}\right) \tag{8}$$

To calculate the magnetic force, the Lorentz's force equation is used as follows:

$$\mathbf{f} = \mathbf{J} \times \mathbf{B} \tag{9}$$

Table 1 Electrical and mechanical properties of parts in EMF process

	part	Material	Element type	Electrical resistivity [Ωm]	Relative permeability	Poison's ratio	Elastic modulus (Pa)
1	Coil	Cu	CIRCU124 PLANE53	1.72 e−8	1	–	–
2	Workpiece	Al	PLANE13	5 e−8	1	0.3	70e9
3	Die	Steel	PLANE13	17 e−8	10	–	3e20
4	Surrounding air	Air	INFIN110 PLANE53	–	1	–	–

Table 2 Physical and mechanical properties of AA 6061-T6 tube workpiece at two strain rates

	Strain rate [s^{-1}]	Young modulus, E, [GPa]	Yield strength [MPa]	U.T.S. [MPa]	Elongation [%]	Density [kg/m^3]	Melting temp [°C]
1	10^{-3}	67.506	302.94	311.4	11.64	2790	620
2	1	67.712	308.65	316.2	9.33	2790	620

But in this problem, Lorentz force density has radial and an axial component as

$$\begin{aligned} f_r &= J_\theta B_z \\ f_z &= -J_\theta B_r \end{aligned} \tag{10}$$

And the corresponding magnetic pressure is evaluated by integration and is defined by

$$\begin{aligned} P_r &= \int_{z=0}^{z=h} f_r dz \\ P_z &= \int_{z=0}^{z=h} f_z dz \end{aligned} \tag{11}$$

where h is the thickness of the tube.

By solving these nonlinear partial differential equations (PDE), magnetic field density and Lorentz body force could be calculated. Regarding that it is difficult to solve these equations analytically, numerical methods should be used. Numerical methods, as well as commercial electromagnetic software can be incorporated to solve these equations. Furthermore, applying these transient forces to a workpiece and calculating deformation shape is not easy, and it is usually simulated by numerical techniques.

3 Experimental tests

Experimental test setup which is shown in Fig. 2 consists of a die (1), forming coil (2), spark gap switch (3), a capacitor bank (4), power supply (5), and control unit (6). In addition, tube (1), die (2), and forming coil (3) are shown separately in Fig. 3. The tube should be placed over the die and then both should be placed in the coil to complete the setup. Furthermore, a cap is screwed over the coil to fasten the tube and prevent the possible pull-out of the workpiece from the coil. Aluminum tube workpieces with 47 mm inner diameter, 50 mm tube length, and 0.625 mm thickness are used in experimental tests. Conical field shaper setup and a coil with inner diameter of 100 mm are shown in Fig. 4. Electrical and physical properties of parts in this EMF process are presented in Table 1. Physical and mechanical properties of tube material, AA 6061-T6, tested at two different strain rate and the results are shown in Table 2. These tests performed on a Gotech Universal Testing Machine (model TCS-2000) at room temperature of 23 °C. The tensile modulus was obtained by an extensometer at tensile elongation of 1 %. The capacitor bank is 256 μF and discharge voltage varies from 4.3 to 5.5 kV. In this study, two coils were used and corresponding parameters are shown in Table 3.

Current variations through discharged capacitor bank were measured by the Rogowsky coil.

Thickness variations in experimental tests were measured before and after forming by the ultrasonic thickness instrument, PANAMETRICS 25DL PLUS. Since it was difficult to measure the thickness at curved areas with ultrasonic probe, these areas were tested by a micrometer with two spherical faces.

All EMF experimental tests used in this paper are summarized in Table 4. In this table, purpose of experiments, number of repetitions, and process parameters are mentioned. As indicated in this table, one series of experimental tests is done to verify predicted thickness. Another series is done to verify predicted radial strain. And last experimental tests are done to investigate effect of field shaper.

4 Simulation of EMF process

The simulation of EMF includes electric, magnetic, and structural coupled analysis. The coupling of both electromagnetic and mechanical fields is one of the main problems in the theoretical study of EMF. Both problems had to be solved by numerical techniques, but there was no single commercial software to solve both of them simultaneously. Therefore, magnetic forces were calculated from electromagnetic FE analysis. Then, the forces were applied to the workpiece in

Table 3 Characteristics of coils

Coil's name	Inner diameter (mm)	Turns (N)	Height (mm)	Wire diameter (mm)	Wire insulation thickness (mm)	Material
C53	53	9	30	5	0.40	Cu
C100	100	9	30	5	0.40	Cu

Table 4 Experimental test conditions

	Test purpose	Voltage [kV]	Repetition no.	Other condition
1	Thickness verification	4.3	3	Thickness 640 and 625 μm
2	Strain verification	4.3, 5.1, 5.16, 5.3	2	–
3	Effect of field shaper	4.1, 4.3, 4.5	2	–

another structural FE analysis. Electromagnetic system details of the FEM model are shown in Fig. 5. An axi-symmetric configuration was assumed for the EMF model. The magnetic pressure was estimated by neglecting the influence of tube velocity on the magnetic field. The temperature dependence of material properties is also ignored, due to a slight increasing of temperature in experimental tests.

In this study, a modified loose-coupled model is used to simulate the EMF process, as shown in Fig. 6. In this method, total simulation time is divided into several steps. In each step, the transient electromagnetic forces are calculated from the electromagnetic model, which are then used as the input load to simulate high velocity deformation of tube from the mechanical model. At first of each step, time air gap between tube and the coil, as shown in Fig. 5, is increased according to the deformation results. Then, the transient magnetic forces are calculated again based on the changed tube geometry in the next time step. The electromagnetic model is updated at 5 μs intervals. Thus, in this method, the effect of tube deformation on the electromagnetic geometry is taken into account in electromagnetic model, by which the predicted dimensional accuracy is improved.

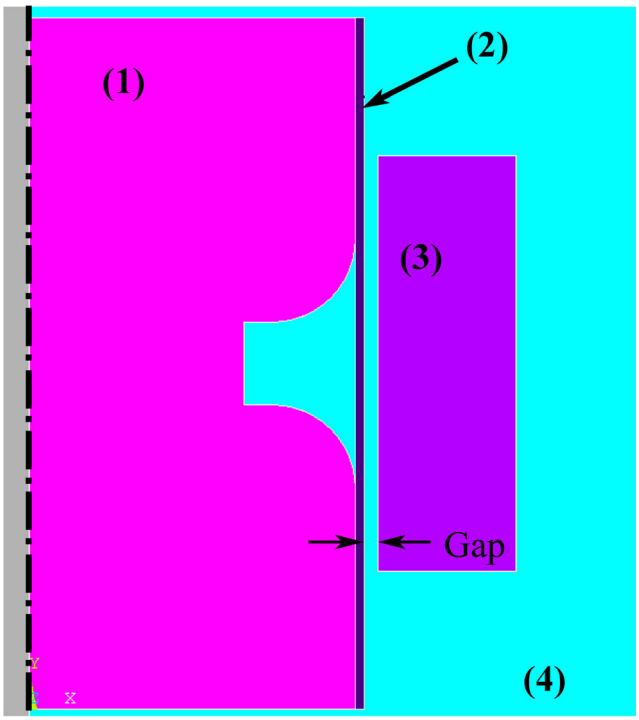

Fig. 5 Die (*1*), tube (*2*), coil (*3*), and surrounding air (*4*) arrangement in the FEM model

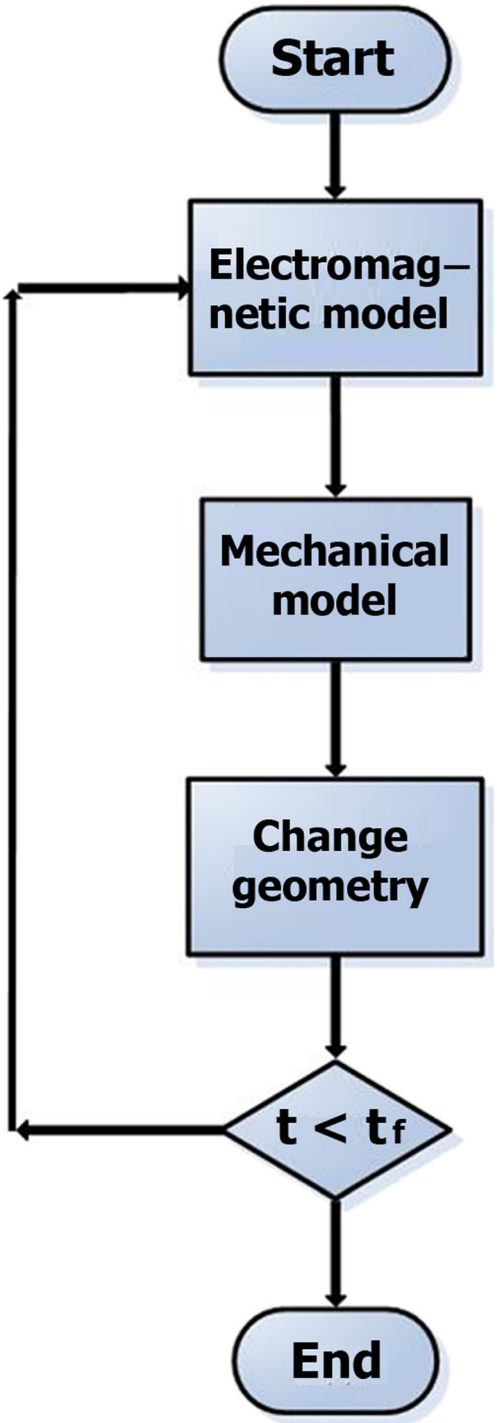

Fig. 6 Flowchart of modified loose-coupled simulation

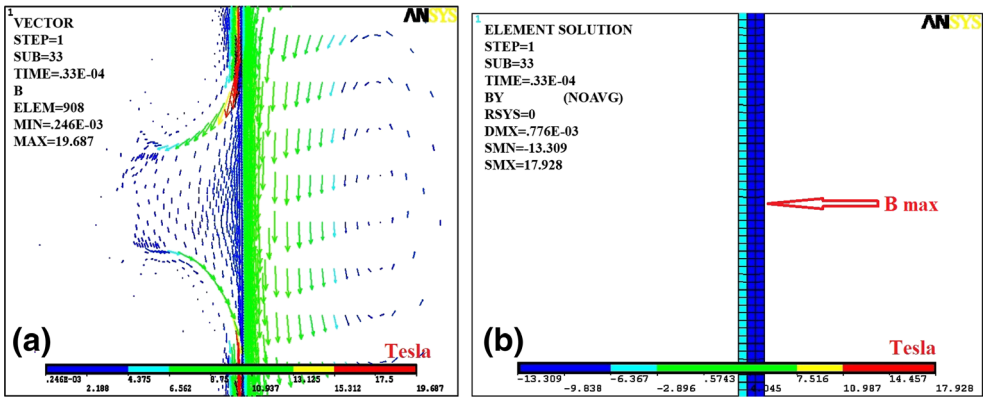

Fig. 7 Magnetic flux density, B [Tesla], at 5.3 kV discharge voltage for **a** forming area and **b** tube workpiece

4.1 Simulation of electromagnetic part

Electromagnetic inward tube forming was simulated with commercial ANSYS 15.0 software. In the axi-symmetric model, four element types with four material types including coil, workpiece, die, and surrounding air were used, the characteristics of which are presented in Table 1. Tube material in this electromagnetic model is assumed to be elastic. Magnetic flux density in forming area and tube workpiece, from electromagnetic analysis, are shown in panels a and b of Fig. 7, respectively. It is seen that maximum flux density in tube is about −13.3 Tesla at the tip of the bead. Negative sign in −13.3 Tesla is related to magnetic field direction. The 17.9 Tesla is related to an element at the end of the tube workpiece and is noise, which should not be considered in next calculations. The electromagnetic load curves applied in structural analysis is shown in Fig. 8a which are derived from loose-coupled and modified loose-coupled method. The calculated electromagnetic force variation along the tube length for 4.3 kV discharge voltage in ANSYS is presented in Fig. 8b, which are similar to the forces in tube expansion [13]. This figure shows nodal forces along the tube length at 34 μs. The tube length was refined by 300 nodes and the load is applied to the tube workpiece in a sinusoidal form.

In all experimental and numerical tests, values of capacitance, coil area, and coil area coefficient (ratio of effective wire area to the total coil area) were 256 μF, 30×8.6 mm^2, and 0.7, respectively. Air gap and number of windings were 2.4 mm and 9. According to Table 4, experimental tests have been done with several voltages which results of two voltages are shown in Figs. 7 and 8.

4.2 Simulation of mechanical part

Magnetic force distribution calculated from ANSYS simulations was then entered in the commercial ABAQUS/Explicit 6.12 code to calculate final tube shape. An axi-symmetric tube workpiece was modeled by 300 SAX1 elements along tube length. The die was assumed rigid. Coulomb friction factor between the workpiece and die was assumed to be 0.15, and forming time was 34 μs. Physical and mechanical properties of the tube workpiece are shown in Table 2. The material was assumed to follow rate-dependent Johnson-Cook (J-C) model [27]. In the J-C constitutive model represented by Eq. (12), the flow stress is described as a function of strain, strain rate, and temperature to consider work hardening, strain-rate hardening, and thermal softening effects.

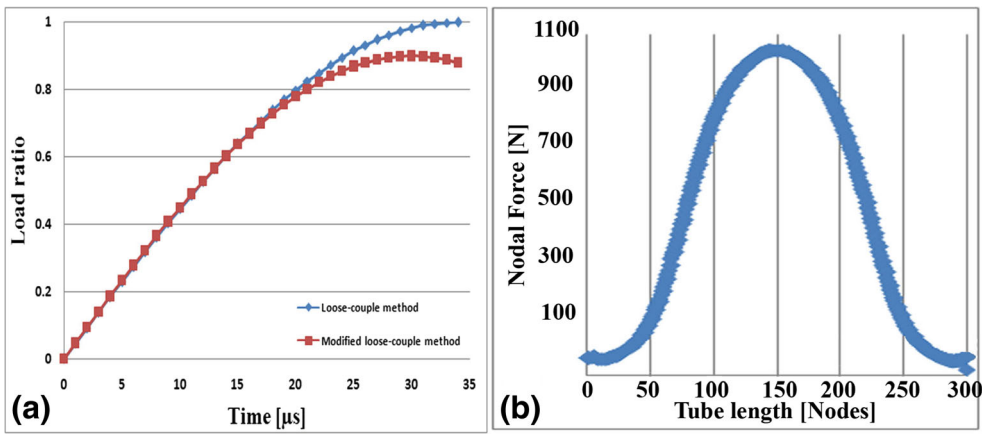

Fig. 8 Electromagnetic load for 4.3 kV discharge voltage (**a**) vs. time and (**b**) along tube length at 34 μs

Table 5 Johnson-Cook equation constants for AA 6061-T6

Material	*A* (MPa)	*B* (MPa)	*C*	*m*	*n*	ε_0
AA 6061-T6	308.65	343	0.011	1.34	0.0201	1

$$\overline{\sigma} = \left[A + B\overline{\varepsilon}^{n}\right].\left[1 + C\ln\left(\frac{\overline{\varepsilon}}{\varepsilon_0}\right)\right].\left[1-\left(\frac{T-T_r}{T_m-T_r}\right)^{m}\right] \quad (12)$$

In this equation, *A*, *B*, *C*, *n*, and *m* are the material constant determined from empirical fit of flow stress data (as a function of strain, strain rate, and temperature). T_r is the room temperature, and T_m is melting temperature of the material, both are assumed constants. The expression in the first set of brackets gives the stress as a function of strain for $\overline{\varepsilon} = 1$ and $T = T_r$. Therefore, the parameter *A* is the initial yield strength of the material at room temperature and $\overline{\varepsilon} = 1$. The expressions in the second and third sets of brackets represent the effect of strain rate and temperature, respectively. The equivalent plastic strain rate $\overline{\varepsilon}^{\cdot}$ is normalized with a reference strain rate, ε_0. While parameter *n* takes into account the strain hardening effect, parameter *m* models the thermal softening effect and parameter *C* represents the strain-rate sensitivity [28, 29]. The J-C model is a well-accepted and numerically robust constitutive material model highly utilized in the modeling and simulation studies. It is noted that Eq. (12) is complete form of materials constitutive equation and for conditions which temperature is not increased significantly, as in these tests, temperature term could be ignored.

The J-C constants for the material used in this study are given in Table 5. These constants are calculated from curve fitting on stress–strain data at $\overline{\varepsilon} = 1$ and from several researchers [27–30].

5 Results and discussion

A tube workpiece and some examples of the formed parts with EMF process are shown in Fig. 9. These figures show that if the discharge voltage increases, bead depth increases up to a specific point. It is seen that if the discharge voltage is so high, it causes the tube to neck and burst (Fig. 9d).

In the previous work [26], after deriving the electric current variations from analytical calculations, both ANSYS simulations and experimental tests were compared at the discharge voltage of 4.3 kV. A good agreement was found between the results. It was seen that the current values calculated from ANSYS and analytical method were a little higher than that of experimental tests.

After transferring and applying electromagnetic forces to the ABAQUS input file, the inward tube forming process was simulated and investigated. As a result of this study, displacements and thickness for 4.3 kV discharge voltage and tube with thickness of 625 μm are shown in panels a and b of Fig. 10, respectively. These results are from ANSYS simulations. Thickness variations at three points has been studied: point 1 at the tip of the bead, point 2 at a point over the die radius with minimum thickness, and point 3 at a point on the tube wall far from the forming zone, which is called feed zone. As shown in Fig. 10a, maximum displacement in tube is at tip of the bead with 1.47 mm.

According to the Fig. 10, the maximum thinning value of 1.4 % occurs over the die radius at point 2. The experimentally measured thinning value at the die radius area was about 1.76 %. Furthermore, maximum simulated and experimental thickening values at the tip of the bead, point 1, were 1.76 and 1.44 %, respectively. Thickness variation profiles along the tube length are shown in Fig. 11 for two tube thicknesses 640 and 625 μm. Each experimental test has been repeated three times. According to this figure, both experimental and simulation thickness variations trends are the same. In both results, the thicknesses increased at the tip of the bead, which are in agreement with Murakoshi et al. study [3], and thicknesses decreased at die radius area. Similar trends have been obtained for the other voltages. These results confirm the FE thickness variations.

Thickness variations of the above-mentioned points located at different tube zones versus time are shown in Fig. 12. As shown in this figure, thickness at point 2 over the die radius is decreased after tube move over die radius and thickness at point 1 at tip of the bead is increased. Circumferential stresses along the tube length for 4.3 kV discharge voltage are shown in Fig. 13. It is seen that thickness at the tip of the bead (point

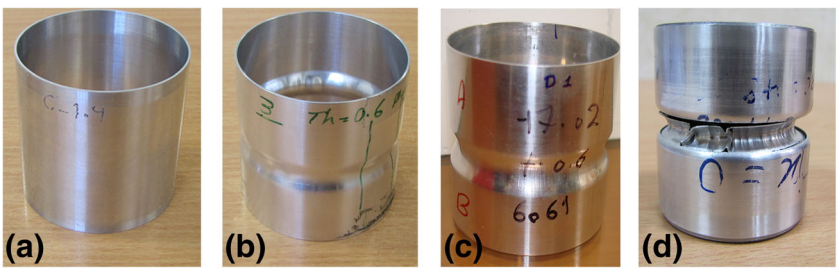

Fig. 9 Parts formed by EMF: **a** tube workpiece; **b** at 4 kV; **c** at 5 kV; **d** burst part, at 5.53 kV

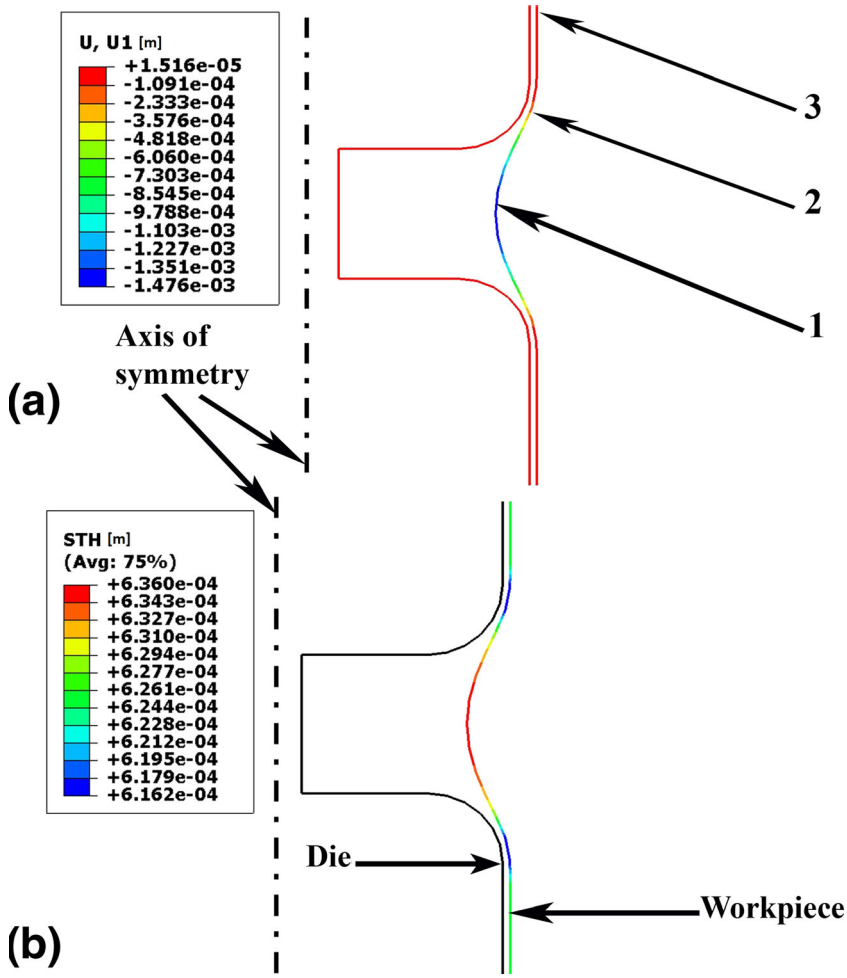

Fig. 10 **a** Displacement (U1) and **b** thickness (STH) at 4.3 kV discharge voltage

1) increases because the radius of this zone has been reduced and this point is under circumferential compressive stress, as shown in Fig. 13. But the thickness of the zone in contact with the die radius (e.g., point 2) first increases and then decreases. This zone is initially under compressive stresses because of the inward movement, and then it is under tension stresses at the end of forming time. The thickness of the feed zone, point 3, does not change during the forming, since this zone is under low tensions.

The thickness variations and displacements at the tip of the bead for 4.3 and 5.3 kV discharge voltage are shown in

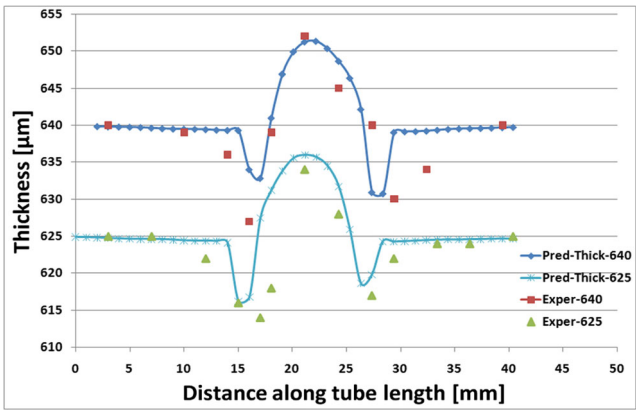

Fig. 11 Predicted and experimental thickness variations at 4.3 kV discharge voltage for two tube thickness 640 and 625 µm

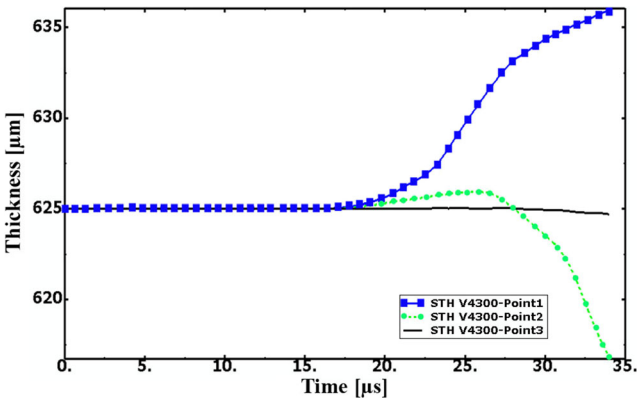

Fig. 12 Thickness variations of workpiece at three elements: 1—point 1 at tip of the bead, 2—point 2 over the die radius, 3—point 3 at tube wall, for 4.3 kV discharge voltage

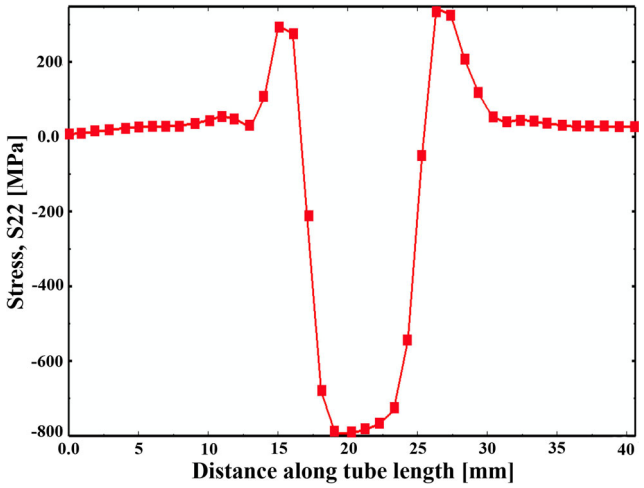

Fig. 13 Circumferential stresses along tube length at 4.3 kV

Fig. 14. It is seen that deformation is negligible till 15 μs; however after this time, the tube starts to deform and the thickness at the tip of the bead, point 1, starts to increase.

Figure 14 shows that if discharge voltage increases, the tube thickness at the tip of the bead behaves differently. Increasing the discharge voltage from 4.3 to 5.3 kV causes a sudden decrease in the thickness of the tip of the bead. This behavior is due to an increase of applied energy. Increase of energy over a critical value will clamp the tube in the feed zone and prevent the inward movement of the tube. Consequently, the tube is locked on the die because of high clamping force and it inhibits the tube movement, leading to a sudden decrease of the thickness at the tip of the bead, point 1. In other word, it is seen that increasing the discharge voltage decreases the thickness over the die radius and reverses the thickening trend at the tip of the bead. This trend was not reported by Murakoshi et al. [3]. Thus, increasing the discharge energy may not be a proper way to increase the deformation in general.

Results of predicted and experimental analyses are summarized in Figs. 15 and 16. It can be seen from Fig. 15 that the absolute of radial strain increases when voltage increases, but

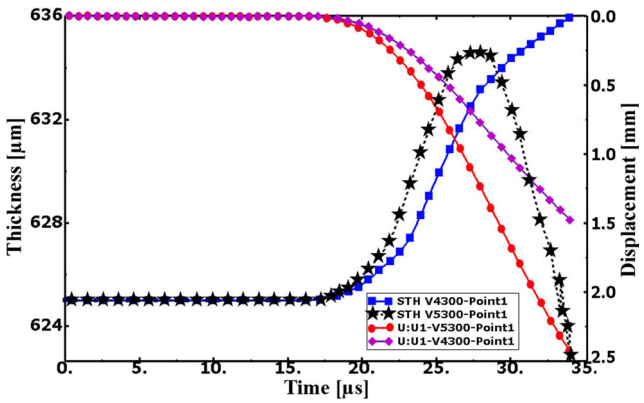

Fig. 14 Thickness variations (STH) and displacement (U1) at the tip of the bead versus time, for 4.3 and 5.3 kV discharge voltages

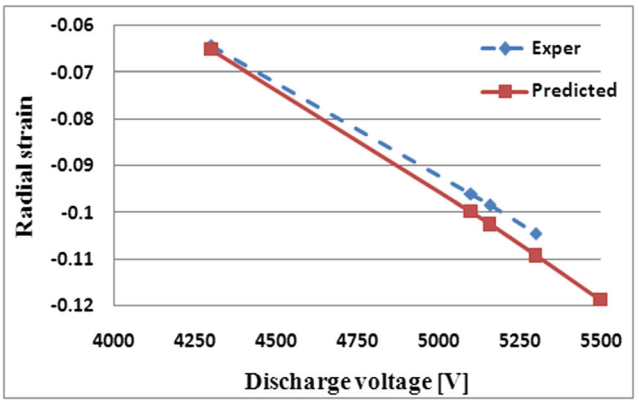

Fig. 15 Experimental and predicted radial strain at tip of the bead

absolute of predicted radial strains are a little more than the experimental ones which are normal because this method does not take into account spring back; furthermore, predicted current and force are a little more than experimental ones [26]. Thus, the employed coupled approach a little overestimates the deformations. When discharge voltage increases, the difference between predicted and experimental radial strain increases. Nonetheless the increasing rate is the same.

Figure 16a, b shows thickness strain at the tip of the bead and die radius area, points 1 and 2, respectively. Figure 16a displays the maximum and minimum experimental thickness strain with the predicted thickness strain variations at the tip of the bead. Thickness is changed in whole circumference at the tip of the bead; thus, this parameter is illustrated as two maximum and minimum lines. In some experimental tests, wrinkling occurred at the tip of the bead; therefore, wrinkling causes to increase and decease the thickness. Although this simulation method could not predict this event and 3D model configuration should be used, this FEM model could predict increasing thickness at tip of the bead. Therefore, this simulation method could not predict all thickness strain variation at the tip of the bead, especially parts which are wrinkled. In this process, as shown in Fig. 16a, b, it is seen that the thickness strain is positive at the tip of the bead and negative over the die radius area, i.e., thickness increases at tip of the bead and decreases over the die radius area. Furthermore, the absolute of thickness strain over the die radius continuously increases with the increase of discharge voltage, but the increasing thickness strain at the tip of the bead stops beyond a specific voltage, i.e., 5.1 kV, and then decreases, due to high clamping force and tube locking, causing necking and tearing of the tube. Hence, experimental thickness strain variations data confirm the simulation results. Figure 17 shows simulated and experimentally obtained displacements at various discharge voltages using C53 coil and also C100 coil with conical field shaper. Results indicate that larger coil could be used with field shaper to form same shape which obtains with smaller coil. Also, it is seen that there is a small difference between displacements of two coils, which is about 4 %. In other word,

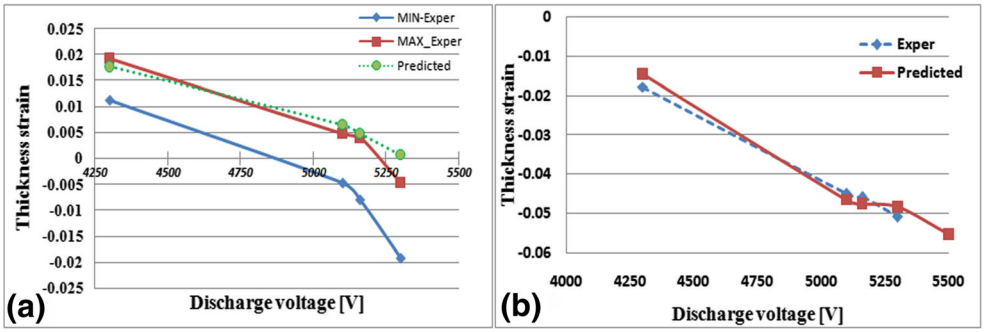

Fig. 16 Experimental and predicted thickness strain at **a** tip of the bead and **b** die radius

displacement at tip of the bead using C100 coil with conical field shaper is 4 % more than direct forming using C53 coil. The reason could be for concentrating energy at the tip of the bead in coil with field shaper.

6 Conclusions

Inward tube electromagnetic forming was investigated both experimentally and numerically in detail. Distribution of magnetic forces was calculated by electromagnetic simulation and applied in ABAQUS/Explicit code to calculate final deformed shape. Modified loose-coupled approach was used to simulate this EMF process, in which the effect of changing tube geometry on the electromagnetic pressure was taken into account. In this modified loose-coupled simulation method, force versus time diagram is modified based on tube geometry. The FE analysis methodology is verified with experimental results such as radial and thickness strain. Specifically following conclusions are derived from this study:

- FE and experimental results show that thickness strain at the tip of the bead increases in this process due to tube diameter reduction and circumferential compressive stresses at this area.
- The thickness strains over the die radius area are negative due to circumferential tension stresses; anyway the absolute of thickness strain continuously increases with an increase of discharge voltage at this area.
- Thickening trend at the tip of the bead is reversed with an increase of discharge voltage, due to the high clamping force and the tube locking.
- Using of C100 coil with conical field shaper at various discharge voltages showed that larger coil could be used with field shaper to form same shape which obtains with smaller coil.

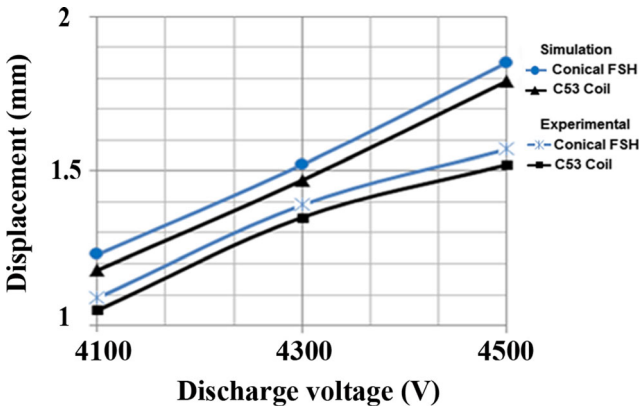

Fig. 17 Simulated and experimentally obtained displacements at various discharge voltages using C53 coil and C100 coil with conical field shaper

Acknowledgments The authors would like to thank the Pulse Niruo Co. for its support. The EMF machine was manufactured by its technical and financial supports.

References

1. Chunfeng L, Zhiheng Z, Jianhui L, Yongzhi W, Yuying Y (2002) Numerical simulation of the magnetic pressure in tube electromagnetic bulging. J Mater Process Technol 123:225–228
2. El-Azab A, Garnich M, Kapoor A (2003) Modeling of the electromagnetic forming of sheet metals: state-of-the-art and future needs. J Mater Process Technol 142:744–754
3. Murakoshi Y, Takahashi M, Sano T, Hanada K, Negishi H (1998) Inside bead forming of aluminum tube by electro-magnetic forming. J Mater Process Technol 80–8:695–699
4. Oliveira DA, Worswick MJ, Finn M, Newman D (2005) Electromagnetic forming of aluminum alloy sheet: free-form and cavity fill experiments and model. J Mater Process Technol 170: 350–362
5. Triantafyllidis N, Waldenmyer JR (2004) Onset of necking in electro-magnetically formed rings. J Mech Phys Solids 52:2127–2148
6. Jimbert P, Eguia I (2015) Improving the electromagnetic forming process efficiency for steel parts by electrolytic coating. DYNA 90(4):383–392. doi:10.6036/7364
7. Bruno EJ (1968) High velocity forming of metals. ASTM Publication, Michigan
8. Correia JPM, Siddiqui MA, Ahzi S, Belouettar S, Davies R (2008) A simple model to simulate electromagnetic sheet free bulging process. Int J Mech Sci 50:1466–1475
9. Mamalis AG, Manolakos DE, Kladas AG, Koumoutsos AK (2004) Electromagnetic forming and powder processing: trends and developments. Appl Mech Rev 57:299–324
10. Psyk V, Risch D, Kinsey BL, Tekkaya AE, Kleiner M (2011) Electromagnetic forming—a review. J Mater Process Technol 211:787–829

11. Takatsu N, Kato M, Sato K, Tobe T (1988) High speed forming of metal sheets by electromagnetic forces. Jpn Soc Mech Eng Int J 60: 142–148
12. Cui X, Mo J, Xiao Sh DE, Zhao J (2011) Numerical simulation of electromagnetic sheet bulging based on FEM. Int J Adv Manuf Technol. doi:10.1007/s00170-011-3273-y
13. Cui X, Mo J, Han F (2012) 3D Multi-physics field simulation of electromagnetic tube forming. Int J Adv Manuf Technol 59:521–529. doi:10.1007/s00170-011-3540-y
14. Bay F, Labbe V, Favennec Y, Chenot JL (2003) A numerical model for induction heating processes coupling electromagnetism and thermo mechanics. Int J Numer Methods Eng 58:839–867
15. Imbert JM, Winkler SL, Worswick MJ, Oliveira DA, Golovashchenko S (2004) Numerical study of damage evolution and failure in an electromagnetic corner fill operation. Proceedings of the 8th Int conference on numerical methods in industrial forming processes, NUMIFORM 2004, Columbus:1833–1838
16. Wang L, Chen ZY, Li CX, Huang SY (2006) Numerical simulation of the electromagnetic sheet metal bulging process. Int J Adv Manuf Technol 30:395–400
17. Li F, Mo J, Zhou H, Fang Y (2013) 3D Numerical simulation method of electromagnetic forming for low conductive metals with a driver. Int J Adv Manuf Technol 64:1575–1585. doi:10.1007/s00170-012-4124-1
18. Al-Hassani STS (1975) Magnetic pressure distribution in the sheet metal forming. Electrical Methods of Machining, Proceedings of the Forming and coating conference, Institute of electrical engineering:1–10
19. Pérez I, Aranguren I, González B, Eguia I (2009) Electromagnetic forming: a new coupling method. Int J Mater Form 2:637–640
20. Siddiqui MA, Correia JPM, Ahzi S, Belouettar S (2008) A numerical model to simulate electromagnetic sheet metal forming process. Int J Mater Form 1:1387–1390
21. Cui X, Mo J, Li J, Huang L, Zhu Y, Li ZW, Zhong K (2013) Effect of second current pulse and different algorithms on simulation accuracy for electromagnetic sheet forming. Int J Adv Manuf Technol 68:1137–1146
22. Haiping Y, Chunfeng L, Jianghua D (2009) Sequential coupling simulation for electromagnetic–mechanical tube compression by finite element analysis. J Mater Process Technol 209:707–713
23. Bartels G, Schatzing W, Scheibe HP, Leone M (2009) Comparison of two different simulation algorithms for the electromagnetic tube compression. Int J Mater Form 2(1):693–696
24. Cao Q, Li L, Lai Z, Zhou Z, Xiong Q, Zhang X, Han X (2014) Dynamic analysis of electromagnetic sheet metal forming process using finite element method. Int J Adv Manuf Technol 74:361–368
25. Vivek A, Kim KH, Daehn GS (2010) Simulation and instrumentation of electromagnetic compression of steel tubes. J Mater Process Technol. doi:10.1016/j.jmatprotec.2010.08.023
26. Fallahi AA, Ebrahimi HH, Farzin M (2012) Numerical and experimental investigation of inward tube electromagnetic forming—electromagnetic study. Adv Mater Res 383–390:6710–6716. doi:10.4028/www.scientific.net/AMR.383-390.6710
27. Dariani BM, Liaghat GH, Gerdooei M (2009) Experimental investigation of sheet metal formability under various strain rates. Proc IMechE Vol 223 Part B: J Engineering Manufacture IMechE 2009:1–10
28. Johnson GR and Cook WH (1983) A constitutive model and data for metals subjected to large strains, high strain rates and high temperatures. In Proc 7th Int Symposium on Ballistics 541–547
29. Lesuer DR, Kay GJ, LeBlanc MM (2001) Modeling large-strain, high-rate deformation in metals. Technical Report UCRL-JC-134118, Lawrence Livermore National Laboratory, Livermore
30. Corbett BM (2006) Numerical simulations of target hole diameters for hypervelocity impacts into elevated and room temperature bumpers. Int J Impact Eng 33:431–440